Towards standardization of tau PET imaging corresponding to various tau PET tracer: multi-center phantom study

Kei Wagatsuma (wagatsuma@pet.tmig.or.jp)
Kitasato University https://orcid.org/0000-0001-7067-9758
Kenta Miwa
Fukushima Medical University
Go Akamatsu
National Institutes for Quantum Science and Technology
Tehsho Yamao
Fukushima Medical University
Yuto Kamitaka
Tokyo Metropolitan Institute of Gerontology
Minoru Sakurai
Nippon Medical School
Naotoshi Fujita
Nagoya University Hospital
Kohei Hanaoka
Kindai University
Hiroshi Matsuda
Fukushima Medical University
Kenji Ishii
Tokyo Metropolitan Institute of Gerontology

Research Article

Keywords: Alzheimer disease, Harmonization, Neurodegeneration, Quantitation, Standardization

Posted Date: March 24th, 2023

DOI: https://doi.org/10.21203/rs.3.rs-2712659/v1

Version of Record: A version of this preprint was published at Annals of Nuclear Medicine on May 27th, 2023. See the published version at https://doi.org/10.1007/s12149-023-01847-8.

Abstract

Objective: Tau positron emission tomography (PET) imaging is a recently developed non-invasive tool that can detect the density and extension of tau neurofibrillary tangles. Tau PET tracers have been validated to harmonize and accelerate their development and implementation in clinical practice. Whereas standard protocols including injected dose, uptake time, and duration have been determined for tau PET tracers, reconstruction parameters have not been standardized. The present study conducted phantom experiments based on tau pathology to standardize quantitative tau PET imaging parameters and optimize reconstruction conditions of PET scanners at four Japanese sites according to the results of phantom experiments.

Methods: The activity of 4.0 and 2.0 kBq/mL for 3D Hoffman brain and cylindrical phantoms, respectively was estimated from published studies of brain activity using [^{18}F]flortaucipir, [^{18}F]THK5351, and [^{18}F]MK6240. We developed an original tau-specific volume of interest (VOI) template for the brain based on pathophysiological tau distribution in the brain defined as Braak stages. We acquired brain and cylindrical phantom images using four PET scanners. Iteration numbers were determined as contrast and recover coefficients (RCs) in grey (GM) and white (WM) matter, and the magnitude of the Gaussian filter was determined from image noise.

Results: Contrast and RC converged at ≥ 4 iterations, the error rates of RC for GM and WM were < 15% and 1%, respectively, and noise was < 10% in Gaussian filters of 2–4 mm in images acquired using the four scanners. Optimizing the reconstruction conditions for phantom tau PET images acquired by each scanner, improved contrast and image noise.

Conclusions: The phantom activity was comprehensive for first- and second-generation tau PET tracers. The mid-range activity that we determined could be applied to later tau PET tracers. We propose an analytical tau-specific VOI template based on tau pathophysiological changes in patients with AD to standardize tau PET imaging. Phantom images reconstructed under the optimized conditions for tau PET imaging achieved excellent image quality and quantitative accuracy.

Introduction

Alzheimer disease (AD) is the most prevalent cause of dementia, accounting for 60–80% of cognitively impaired patients. Pathological changes in the brain with AD are characterized by extracellular amyloid β (Aβ) aggregates, intracellular tau neurofibrillary tangles and the neuron death [1]. Abnormal proteins such as Aβ and tau accumulate in the brain before symptoms appear. The National Institute of Aging-Alzheimer's Association (NIA-AA) proposed a research framework to define AD as a biological construct rather than a clinical consequence in its 2018 update. This framework was based on the AT(N) model, which describes patients based on AD-specific biomarkers targeting Aβ (A), tau (T), and neurodegeneration (N) [2]. A more accurate characterization of AD using these biomarkers should provide

an understanding of the sequence of events leading to the cognitive impairment that is associated with AD, as well as the multifactorial etiology of dementia.

Tau PET imaging is a more recently developed tool that can minimal invasively assess tau pathophysiology. The distribution of tau neurofibrillary tangles is classified as Braak stages defined at autopsy [3, 4]. Tau PET images have revealed that the cortical uptake of tau PET tracers not only corresponds to a Braak stage but is also associated with markers of neural injury or cortical grey matter atrophy [5–9]. Tau PET images are useful to predict AD progression for staging because the density, extension, and regional distribution of tau deposits can be determined [10]. Several tau PET tracers such as [^{18}F]flortaucipir (also known as [^{18}F]AV1451), [^{11}C]PBB3, [^{18}F]THK5351, [^{18}F]GTP1, [^{18}F]MK6240, [^{18}F]PI2620, [^{18}F]PM-PBB3, [^{18}F]RO948, and [^{18}F]S-16) have already been assessed in proof-of-concept studies [11–18]. The first-generation of tau PET tracers [^{18}F]flortaucipir, [^{18}F]THK5351, and [^{11}C]PBB3 were thought to be tau specific, but some binding was off-target [19–22]. Second-generation tau PET tracers had better affinity and more selectivity that resulted in reduced off-target binding [19]. However, the injected dose, uptake duration, and scan duration varied among these tracers [11–17, 23, 24]. Images of patients with AD also differed from between first- and second-generation tau PET tracers due to variations in chemical structures and image acquisition parameters [19].

Longitudinal and cross-sectional standardization of tau PET images was therefore required. Thus, the Japanese Society of Nuclear Medicine (JSNM) proposed phantom test procedures and criteria to standardize brain [^{18}F]FDG and amyloid PET imaging [25]. Several studies then determined optimal reconstruction conditions for brain [^{18}F]FDG and amyloid PET imaging using an iterative reconstruction method based on the JSNM phantom test criteria [26, 27]. The FDA approved [^{18}F]flortaucipir as the first tau PET ligand in 2020 [28]. The Molecular Imaging-based Precision Medicine Task Group published an international consensus regarding [^{18}F]flortaucipir PET imaging protocols and results for clinical purposes [29]. Although the Task Group recommended three-dimensional ordered-subset expectation-maximization (3D-OSEM) as the reconstruction algorithm for [^{18}F]flortaucipir PET images, reconstruction parameters such as iterations and subsets were not mentioned. The Alzheimer's Disease Neuroimaging Initiative (ADNI)-3 provided reconstruction parameters for [^{18}F]flortaucipir PET imaging for PET scanners from all vendors. However, they proposed identical reconstruction conditions for [^{18}F]FDG, amyloid, and [^{18}F]flortaucipir imaging [30]. Tau PET imaging to evaluate the progression of tau tangles should be able to detect early tau deposition in the medial temporal lobe and define an accurate threshold of tau positivity [4, 19, 31–33]. Therefore, the reconstruction conditions for tau PET imaging using [^{18}F]FDG, or amyloid should not be identical. They should be concomitantly optimized with scan protocols for tau PET tracers. However, the methodology of phantom test to determine and optimize reconstruction conditions for tau PET imaging has not been addressed compared with brain [^{18}F]FDG or amyloid PET imaging.

This Japanese multicenter study aimed to develop an objective methodology for phantom test protocols that could determine dedicated reconstruction parameters to standardize tau PET imaging. We developed an analytical volume of interest (VOI) template based on the pathophysiological characteristics of tau

deposition. We then validated it using phantom test procedures and a VOI analytical method, then optimized the reconstruction conditions for tau PET imaging.

Materials And Methods

Determination of phantom conditions

Here, we initially estimated the activity of [^{18}F]flortaucipir, [^{18}F]THK5351, and [^{18}F]MK6240 tau PET tracers in the brain with reference to published scan parameters [34–36]. The conventional injected doses (MBq) and uptake durations (min) were 370 and 70, 185 and 40, and 185 and 90 for [^{18}F]flortaucipir, [^{18}F]THK5351, and [^{18}F]MK6240, respectively [34–36], and the acquisition duration was 20 min for all three tracers. The estimated whole brain activity at the start of PET acquisition was 4.0, 1.0, 1.5 MBq for [^{18}F]flortaucipir, [^{18}F]THK5351, and [^{18}F]MK6240, respectively. The standard brain volume was equivalent to 1,200 mL. The activity concentration in a normal brain was 3.33, 0.83, 1.25 kBq/mL for [^{18}F]flortaucipir, [^{18}F]THK5351, and [^{18}F]MK6240, respectively.

We then calculated activity in the phantom based on estimated brain activity. The distribution of tau PET tracers in the brain corresponded to that of tau deposition defined in terms of Braak stages [3, 4]. Alzheimer disease can be detected early if PET imaging can detect local tau accumulation in the medial temporal lobe. Local accumulation is underestimated if a Hoffman 3D brain phantom (Data Spectrum Corporation, Hillsborough, NC, USA) contains whole brain activity that was described in previous paragraph. Therefore, we considered that the target (local accumulation) and reference regions could be mimicked by the Hoffman 3D brain phantom and a cylindrical phantom (Itoi Plastics Co. Ltd., Kobe, Japan), respectively, containing different amounts of activity. The average activity concentration of the three tau PET tracers in the whole brain was ~ 2.0 kBq/mL. The volume of the cylindrical phantom and the amount of activity in it were 6 L and 12.0 MBq, respectively, at the start PET image acquisition. The concentration of activity in the brain phantom was taken as the standardized uptake value ratio (SUVR) in the medial temporal lobe. The SUVR of the medial temporal lobe or hippocampus calculated from the activity concentrations of [^{18}F]flortaucipir, [^{18}F]THK5351, and [^{18}F]MK6240 in the cerebellar cortex as a reference region was ~ 2.0 [37–44]. Thus, the concentration of activity in the brain phantom was twice that in the cylindrical phantom. The volume of the brain phantom and the activity in it were 1.2 L and 4.8 MBq, respectively, at the start of PET acquisition.

Characteristics of equipment at four sites

Radioactivity in the phantoms was quantified using two brands of dose calibrators (Nippon RayTech Co., Ltd., Tokyo, Japan and Capintec Inc., Ramsey, NJ, USA), and four PET/computed tomography (CT) scanners (one from GE Healthcare, Milwaukee, WI, USA and three from Siemens Healthineers, Erlangen, Germany). Table 1 shows the PET/CT systems and dose calibrators. Reconstruction conditions except for the iterations and the Gaussian filter (Table 1) proceeded under the clinical conditions for brain PET

examinations at each site. The performance of the PET/CT scanners has been described elsewhere [45–48].

Table 1
Characteristics of equipment at four sites

Site	PET		Dose calibrator (Manufacture)
	Scanner (Manufacture)	Reconstruction conditions	
NUH	Biograph 16 (SIEMENS)	3D-OSEM; subset, 16; pixel size, 2 mm	IGC-7F (Aloka)
QST	Biograph mCT Flow (SIEMENS)	3D-OSEM + TOF; subset, 21; pixel size, 2 mm	IGC-3 (Aloka)
NMS	Biograph Vision (SIEMENS)	3D-OSEM + TOF; subset, 5; pixel size, 2 mm	CRC-55tR (Capintec)
TMIG	Discovery MI (GE Healthcare)	3D-OSEM + TOF; subset, 16; pixel size, 2 mm	CRC-55tR (Capintec)

NMS, Nippon Medical School; NUH, Nagoya University Hospital; PET, positron emission tomography; QST, National Institutes for Quantum Science and Technology; TMIG, Tokyo Metropolitan Institute of Gerontology; TOF, time-of-flight; 3D-OSEM, three-dimensional ordered subset expectation maximization.

Phantom experiment

Computed tomography images were acquired from all scanners to correct attenuation, scatter and other issues except for the point-spread function. Thereafter, images were acquired from the brain and cylindrical phantoms initially containing 4.8 and 12.0 MBq of [^{18}F]FDG, respectively, for 20 min based on the protocols for [^{18}F]flortaucipir, [^{18}F]THK5351, and [^{18}F]MK6240.

Creation of a VOI template for brain phantom images

We created a VOI template (Fig. 1) to optimize tau PET images based on Braak stages using PMOD v. 3.8 (PMOD Technologies LLC, Zurich, Switzerland). We then analyzed tau PET images acquired from the brain phantom. Each VOI was placed according to the distribution of tau pathology in patients with AD. The locations and amounts of voxels in the inferotemporal cortex, lateral temporal lobe, precuneus, white matter (WM), and cerebellar cortex were 357, 375, 365, 576, and 769 voxels, respectively. The inferotemporal cortex, lateral temporal lobe and precuneus comprised the grey matter (GM) VOI and the cerebellar cortex was the reference VOI.

Image analysis

Determination of iteration number

The data acquired from brain phantom images were reconstructed with 1–10 iterations and no post filter. Mean activity concentrations in the GM and WM were measured using the VOI template. The ratio of grey-to-white matter contrast (contrast [%]) and the recovery coefficient (RC) at the GM and WM were calculated as:

$$Contrast\,(\%) = \frac{(GM_p/WM_p - 1)}{(GM_d/WM_d - 1)} \times 100$$

,

where GM_p and WM_p in the brain, and GM_d and WM_d in the digital brain phantom PET images are GM and WM activities respectively, in VOIs. The GM_d and WM_d values provided a true gray-to-white ratio of 4 and were applied to the image co-registered to the digital phantom. Contrast was measured using PMOD v. 3.8.

The RC at GM and WM was defined as the image-derived mean activity concentration determined as contrast divided by the activity concentration of the stock solution in the brain phantom. The activity concentration in the brain phantom derived from net phantom activity (measured using a dose calibrator at each site), divided by the fillable volume (1.14 L) of the brain phantom. The activity concentration in WM was 25% of that in GM. The convergence of contrast or RC in 1–10 iterations was defined as optimal iteration for tau PET imaging.

Determination of Gaussian filter magnitude

Data acquired from the cylindrical phantom was reconstructed using the optimal number of iterations determined as contrast (%), RC, and Gaussian filter magnitudes of 0–10 mm at full width at half maximum (FWHM). A large circular ROI (13 cm diameter; nROI) was placed on the center of the cylindrical phantom image to evaluate noise as a coefficient of variation (CV) calculated as:

$$CV\,(\%) = \frac{SD_{nROI}}{nROI_{mean}} \times 100$$

,

where SD_{nROI} is the standard deviation of the voxel numbers within the nROI, and $nROI_{mean}$ is mean nROI activity. The optimal magnitudes of Gaussian filters were determined from CVs < 15%.

Results

Numbers of iterations

Figure 2 shows contrast in the four scanners as a function of the number of iterations. Contrast increased along with iteration numbers and converged at ≥ 4 iterations. Contrast at convergence points was 85%

and 70–75% in two scanners each.

Figure 3 shows the RC in four scanners as a function of iteration numbers. The RCs at GM and WM respectively increased and decreased with increasing numbers of iterations. The RCs at GM and WM converged iteration ≥ 4. The RC in GM underestimated (RC = 1.0), whereas that in WM overestimated (RC = 0.25) the true activity. The RC error from true activity was − 15% for GM and 15% for WM.

Determination of Gaussian filter magnitude

Figure 4 shows image noise in four scanners as a function of Gaussian filter magnitudes. The CV decreased as the filter magnitude increased. Two images each acquired using two scanners each had less (CV = 10–15%) and more (CV = 25%) image noise. Images from two scanners had CVs < 10% when the Gaussian filter magnitude was 2 or 4 mm at FWHM.

Phantom images

Figure 5 shows the physical indices of brain and cylindrical images acquired using four scanners under tau-specific optimized reconstruction conditions. Contrast and CV were respectively, 67.2% and 8.6% for the Biograph 16, 73.8% and 7.3% for the Biograph mCT Flow, 75.3% and 4.9% for the Biograph Vision, and 70.2% and 6.9% for the Discovery MI. The images have good contrast and low image noise.

Discussion

The methodology required to determine reconstruction conditions for tau PET imaging has not been established and standardized. We mimicked the brain activity of three tau PET tracers using brain and cylindrical phantoms. We developed a VOI template to analyze tau PET images based on the pathophysiological distribution of tau in the brain. We determined the number of iterations and Gaussian filter parameters as two of the reconstruction conditions for different PET/CT scanners at four Japanese institutions.

We estimated the brain activity of [^{18}F]flortaucipir, [^{18}F]THK5351, and [^{18}F]MK6240 from published data at the start of image acquisition to define phantom conditions. The process referred to JSNM phantom test procedures to define brain [^{18}F]FDG activity using four amyloid PET tracers [25]. We used brain uptake and kinetic information from dosimetry studies of several tau PET tracers to estimate the activity of tau PET tracers in the brain [34–36]. We determined the activity of the three tau PET in the cylindrical and brain phantoms were 2.0 and 4.0 kBq/mL, respectively. However, experimental conditions from phantoms should be established for each individual tau PET tracer. If images are acquired using more than one tau PET tracer, several experiments are needed to optimize the reconstruction condition for each of them. Several complex experiments can lead to measurement error while concomitantly exposing operators to needless amounts of radiation. We considered that the phantom experiment to determine the activity condition of three tau PET tracers was reasonable and could be generalized to standardize tau PET imaging protocols. The convergence of PET images using an iterative reconstruction algorithm

depends on the target activity, the acquired PET counts, and the target size or shape. We previously found that the convergence rate of contrast was independent of target activity because the conditions of the iterative reconstruction algorithm were the same regardless of phantom activity [26, 27]. The high levels of whole-brain activity in tau PET images in first generation tau PET tracers due to non-specific brain uptake were decreased in second generation tau PET tracers. The activity of 2.0 kBq/mL herein was in the mid-range of brain activity in both generations of tau PET tracers. Our phantom experiment objectively determined appropriate reconstruction conditions for tau PET images because mid-range activity can be applied to more recent tau PET tracers. The activity in the brain phantom containing 4.0 kBq/mL was equivalent to an SUVR of ~ 2.0 at the medial temporal lobe and hippocampus in a patient with AD [37–44]. The role of tau PET imaging is to define the density and extent of tau deposition in patients with AD. Therefore, tau PET imaging should contribute to the early diagnosis of AD based on the detection tau deposition in the entorhinal cortex or hippocampus corresponding to an early Braak stage [31–33]. Tau pathology visualized as [^{18}F]flortaucipir accumulation was visually undetectable in Braak stage I–III [49, 50]. The cut-off SUVR required to distinguish Braak stages I–III from IV is 1.29 [50]. Second-generation tau PET tracers could track longitudinal tau accumulation in asymptomatic and symptomatic AD [51, 52]. The cut-off of SUVR in second generation tau PET tracers to distinguish AD from non-AD is 1.35 [53]. We propose a phantom activity rate of 2.0. However, we plan to re-evaluate the phantom activity to validate the early detection of tau accumulation.

Our new tau-specific VOI template for analyzing phantom tau PET images based on the Braak stages covered the inferotemporal cortex, lateral temporal lobe, precuneus, white matter (WM), and cerebellar cortex that are frequently characterized by tau deposition in patients with AD. The six Braak stages were categorized based on the distribution and developmental sequences of lesions. The tau PET-specific VOI corresponded to Braak stages I/II, III/IV, and V/VI that were anatomically defined as trans-entorhinal, limbic, and isocortical. Other clinical studies have analyzed tau PET images using an AD-signature temporal meta-ROI or an anatomical definition of VOI also based on Braak stages [41, 44, 54–57]. Dore *et al*. developed a universal cortical tau mask comprising the tau PET ligands [^{18}F]flortaucipir, [^{18}F]GTP1, [^{18}F]MK6240, [^{18}F]PI2620, [^{18}F]PM-PBB3, and [^{18}F]RO948 to evaluate tau accumulation during the AD continuum in areas common to tau PET ligands [58, 59].

Optimal reconstruction conditions for tau PET images from four PET/CT scanners were determined as contrast, RC, and image noise calculated from brain and cylindrical phantom images. Images of the brain and cylindrical phantom were acquired with sufficient image quality for visual assessment by physicians. Contrast and RC converged at ≥ 4 iterations regardless of scanner generation or vendor. The convergence rate was equivalent to that in a previous study because it was independent of phantom activity, locations of quantified activity in the phantom, and the shape of the VOI template [26]. Brain PET imaging in dementia has been compared longitudinally or cross-sectionally among patients or with a reference database [8]. The recent Research for life (EARL) study (EANM Research Ltd., Vienna, Austria) investigated the harmonization of image quality and quantitative capability in clinical brain PET images [60]. We used the RC proposed in the EARL study as a quantitation index to harmonize PET images and

validate our method. The RCs in GM and WM were 0.88–1.01 (true value, 1.00) and 0.25–0.27 (true value, 0.25), respectively. Our quantitative capability surpassed that of an earlier study [60]. In particular, the high-end SiPM-PET/CT Biograph Vision scanner, allowed precise quantitation due to the spatial and temporal resolution being better than that of PMT-PET [47]. The RC in the present study decreased the effects of spill-in or -out because our VOIs were separated between GM and WM, unlike those in an earlier study [60]. The image noise (CV) achieved < 10% with Gaussian filters set at 2–4-mm (at FWHM) in four scanners. The acceptance criteria of image quality in the JSNM phantom test procedure for [^{18}F]FDG and amyloid PET imaging has been defined as CV < 15% [25]. Tau PET imaging should be able to detect local tau deposition and warm tau tracer accumulation in small structures or tissues such as the medial temporal lobe [4, 19, 31–33]. Brain activity and PET counts were lower than those of [^{18}F]FDG and [^{18}F]florbetapir [25] in tau images, especially when measured using second generation tracers. Noise on tau PET images caused by statistically fewer PET counts hindered the early detection of local or warm tau depositions. We proposed that image noise should be a CV ≤ 15%.

The present study has some limitations. We did not investigate reconstruction conditions other than iterations and Gaussian filters, and we applied clinical conditions for standard brain PET imaging at each site. The Molecular Imaging-based Precision Medicine Task Group and ADNI-3 respectively recommended pixel sizes of 2–4 and < 2.0 mm to acquire [^{18}F]flortaucipir PET images [29, 30]. The pixel size in four scanners was equivalent to that in previous studies and it was also appropriate in the present study. When pixels ≤ 1.0 mm were used to detect early tau deposition, the Gaussian filter was adjusted to suppress image noise. Another limitation of the present study is that the Hoffman 3D brain phantom simulated the distribution of flow or metabolic tracers in the brain [61]. However, the distribution of tau deposition differs from the flow of metabolic tracers. A tau-specific phantom should be developed to determine optimal qualitative and quantitative reconstruction conditions for tau PET imaging. We selected the Hoffman 3D brain phantom because it is widely available.

Conclusions

We estimated the activity of 4.0 and 2.0 kBq/mL in brain and cylindrical phantoms based on the brain activity of some tau PET tracers that were used in previous tau PET imaging studies. We developed a tau-specific VOI based on tau deposition corresponding to Braak stages. We optimized the reconstruction parameters of iteration numbers and the Gaussian filter magnitude using tau PET images acquired from a phantom by four PET/CT scanners. The image quality and quantitative capability were sufficient under our conditions.

Declarations

Acknowledgments

This study was supported in part by JSPS KAKENHI Grant Number (KW, JP20K16747), the Japanese Government, and an Academic Research Grant from the Japanese Society of Radiological Technology.

References

1. Association As. 2020 Alzheimer's disease facts and figures. Alzheimers Dement. 2020;16(3):391–460.
2. Jack CR Jr, Bennett DA, Blennow K, Carrillo MC, Dunn B, Haeberlein SB, et al. NIA-AA Research Framework: Toward a biological definition of Alzheimer's disease. Alzheimers Dement. 2018;14(4):535–62.
3. Braak H, Alafuzoff I, Arzberger T, Kretzschmar H, Del Tredici K. Staging of Alzheimer disease-associated neurofibrillary pathology using paraffin sections and immunocytochemistry. Acta Neuropathol. 2006;112(4):389–404.
4. Braak H, Braak E. Neuropathological stageing of Alzheimer-related changes. Acta Neuropathol. 1991;82(4):239–59.
5. Cho H, Choi JY, Hwang MS, Kim YJ, Lee HM, Lee HS, et al. In vivo cortical spreading pattern of tau and amyloid in the Alzheimer disease spectrum. Ann Neurol. 2016;80(2):247–58.
6. Johnson KA, Schultz A, Betensky RA, Becker JA, Sepulcre J, Rentz D, et al. Tau positron emission tomographic imaging in aging and early Alzheimer disease. Ann Neurol. 2016;79(1):110–9.
7. Lowe VJ, Wiste HJ, Senjem ML, Weigand SD, Therneau TM, Boeve BF, et al. Widespread brain tau and its association with ageing, Braak stage and Alzheimer's dementia. Brain. 2018;141(1):271–87.
8. Scholl M, Lockhart SN, Schonhaut DR, O'Neil JP, Janabi M, Ossenkoppele R, et al. PET Imaging of Tau Deposition in the Aging Human Brain. Neuron. 2016;89(5):971–82.
9. Schwarz AJ, Yu P, Miller BB, Shcherbinin S, Dickson J, Navitsky M, et al. Regional profiles of the candidate tau PET ligand ^{18}F-AV-1451 recapitulate key features of Braak histopathological stages. Brain. 2016;139(Pt 5):1539–50.
10. Villemagne VL, Dore V, Burnham SC, Masters CL, Rowe CC. Imaging tau and amyloid-beta proteinopathies in Alzheimer disease and other conditions. Nat Rev Neurol. 2018;14(4):225–36.
11. Declercq L, Rombouts F, Koole M, Fierens K, Marien J, Langlois X, et al. Preclinical Evaluation of ^{18}F-JNJ64349311, a Novel PET Tracer for Tau Imaging. J Nucl Med. 2017;58(6):975–81.
12. Harada R, Okamura N, Furumoto S, Furukawa K, Ishiki A, Tomita N, et al. ^{18}F-THK5351: A Novel PET Radiotracer for Imaging Neurofibrillary Pathology in Alzheimer Disease. J Nucl Med. 2016;57(2):208–14.
13. Lu J, Bao W, Li M, Li L, Zhang Z, Alberts I, et al. Associations of [^{18}F]-APN-1607 Tau PET Binding in the Brain of Alzheimer's Disease Patients With Cognition and Glucose Metabolism. Front Neurosci. 2020;14:604.
14. Mueller A, Bullich S, Barret O, Madonia J, Berndt M, Papin C, et al. Tau PET imaging with ^{18}F-PI-2620 in Patients with Alzheimer Disease and Healthy Controls: A First-in-Humans Study. J Nucl Med. 2020;61(6):911–9.

15. Sanabria Bohorquez S, Marik J, Ogasawara A, Tinianow JN, Gill HS, Barret O, et al. [^{18}F]GTP1 (Genentech Tau Probe 1), a radioligand for detecting neurofibrillary tangle tau pathology in Alzheimer's disease. Eur J Nucl Med Mol Imaging. 2019;46(10):2077–89.
16. Shcherbinin S, Schwarz AJ, Joshi A, Navitsky M, Flitter M, Shankle WR, et al. Kinetics of the Tau PET Tracer ^{18}F-AV-1451 (T807) in Subjects with Normal Cognitive Function, Mild Cognitive Impairment, and Alzheimer Disease. J Nucl Med. 2016;57(10):1535–42.
17. Wong DF, Comley R, Kuwabara H, Rosenberg PB, Resnick SM, Ostrowitzki S et al. First in-human PET study of 3 novel tau radiopharmaceuticals: [^{11}C]RO6924963, [^{11}C]RO6931643, and [^{18}F]RO6958948. J Nucl Med. 2018;59(12):jnumed.118.209916.
18. Wood H. Alzheimer disease: [^{11}C]PBB3–a new PET ligand that identifies tau pathology in the brains of patients with AD. Nat Rev Neurol. 2013;9(11):599.
19. Leuzy A, Chiotis K, Lemoine L, Gillberg PG, Almkvist O, Rodriguez-Vieitez E, et al. Tau PET imaging in neurodegenerative tauopathies-still a challenge. Mol Psychiatry. 2019;24(8):1112–34.
20. Lowe VJ, Curran G, Fang P, Liesinger AM, Josephs KA, Parisi JE, et al. An autoradiographic evaluation of AV-1451 Tau PET in dementia. Acta Neuropathol Commun. 2016;4(1):58.
21. Marquie M, Normandin MD, Vanderburg CR, Costantino IM, Bien EA, Rycyna LG, et al. Validating novel tau positron emission tomography tracer [F-18]-AV-1451 (T807) on postmortem brain tissue. Ann Neurol. 2015;78(5):787–800.
22. Ng KP, Pascoal TA, Mathotaarachchi S, Therriault J, Kang MS, Shin M, et al. Monoamine oxidase B inhibitor, selegiline, reduces ^{18}F-THK5351 uptake in the human brain. Alzheimers Res Ther. 2017;9(1):25.
23. Kimura Y, Endo H, Ichise M, Shimada H, Seki C, Ikoma Y, et al. A new method to quantify tau pathologies with ^{11}C-PBB3 PET using reference tissue voxels extracted from brain cortical gray matter. EJNMMI Res. 2016;6(1):24.
24. Young PNE, Estarellas M, Coomans E, Srikrishna M, Beaumont H, Maass A, et al. Imaging biomarkers in neurodegeneration: current and future practices. Alzheimers Res Ther. 2020;12(1):49.
25. Ikari Y, Akamatsu G, Nishio T, Ishii K, Ito K, Iwatsubo T, et al. Phantom criteria for qualification of brain FDG and amyloid PET across different cameras. EJNMMI Phys. 2016;3(1):23.
26. Akamatsu G, Ikari Y, Nishio T, Nishida H, Ohnishi A, Aita K, et al. Optimization of image reconstruction conditions with phantoms for brain FDG and amyloid PET imaging. Ann Nucl Med. 2016;30(1):18–28.
27. Wagatsuma K, Miwa K, Kamitaka Y, Koike E, Yamao T, Yoshii T, et al. Determination of optimal regularization factor in Bayesian penalized likelihood reconstruction of brain PET images using [^{18}F]FDG and [^{11}C]PiB. Med Phys. 2022;49(5):2995–3005.
28. Mattay VS, Fotenos AF, Ganley CJ, Marzella L. Brain Tau Imaging: Food and Drug Administration Approval of ^{18}F-Flortaucipir Injection. J Nucl Med. 2020;61(10):1411–2.

29. Tian M, Civelek AC, Carrio I, Watanabe Y, Kang KW, Murakami K, et al. International consensus on the use of tau PET imaging agent ^{18}F-flortaucipir in Alzheimer's disease. Eur J Nucl Med Mol Imaging. 2022;49(3):895–904.
30. Weber CJ, Carrillo MC, Jagust W, Jack CR Jr, Shaw LM, Trojanowski JQ, et al. The Worldwide Alzheimer's Disease Neuroimaging Initiative: ADNI-3 updates and global perspectives. Alzheimers Dement (N Y). 2021;7(1):e12226.
31. Bischof GN, Dodich A, Boccardi M, van Eimeren T, Festari C, Barthel H, et al. Clinical validity of second-generation tau PET tracers as biomarkers for Alzheimer's disease in the context of a structured 5-phase development framework. Eur J Nucl Med Mol Imaging. 2021;48(7):2110–20.
32. Chiotis K, Dodich A, Boccardi M, Festari C, Drzezga A, Hansson O, et al. Clinical validity of increased cortical binding of tau ligands of the THK family and PBB3 on PET as biomarkers for Alzheimer's disease in the context of a structured 5-phase development framework. Eur J Nucl Med Mol Imaging. 2021;48(7):2086–96.
33. Wolters EE, Dodich A, Boccardi M, Corre J, Drzezga A, Hansson O, et al. Clinical validity of increased cortical uptake of [^{18}F]flortaucipir on PET as a biomarker for Alzheimer's disease in the context of a structured 5-phase biomarker development framework. Eur J Nucl Med Mol Imaging. 2021;48(7):2097–109.
34. Hsiao IT, Lin KJ, Huang KL, Huang CC, Chen HS, Wey SP, et al. Biodistribution and Radiation Dosimetry for the Tau Tracer ^{18}F-THK-5351 in Healthy Human Subjects. J Nucl Med. 2017;58(9):1498–503.
35. Koole M, Lohith TG, Valentine JL, Bennacef I, Declercq R, Reynders T, et al. Preclinical Safety Evaluation and Human Dosimetry of [^{18}F]MK-6240, a Novel PET Tracer for Imaging Neurofibrillary Tangles. Mol Imaging Biol. 2020;22(1):173–80.
36. Golla SSV, Timmers T, Ossenkoppele R, Groot C, Verfaillie S, Scheltens P, et al. Quantification of Tau Load Using [^{18}F]AV1451 PET. Mol Imaging Biol. 2017;19(6):963–71.
37. Chen J, Li Y, Pirraglia E, Okamura N, Rusinek H, de Leon MJ, et al. Quantitative evaluation of tau PET tracers ^{18}F-THK5351 and ^{18}F-AV-1451 in Alzheimer's disease with standardized uptake value peak-alignment (SUVP) normalization. Eur J Nucl Med Mol Imaging. 2018;45(9):1596–604.
38. He M, Baker SL, Shah VD, Lockhart SN, Jagust WJ. Scan-Time Corrections for 80-100-min Standardizetd Uptake Volume Ratios to Measure the ^{18}F-AV-1451 Tracer for Tau Imaging. IEEE Trans Med Imaging. 2019;38(3):697–709.
39. Lockhart SN, Baker SL, Okamura N, Furukawa K, Ishiki A, Furumoto S, et al. Dynamic PET Measures of Tau Accumulation in Cognitively Normal Older Adults and Alzheimer's Disease Patients Measured Using [^{18}F] THK-5351. PLoS ONE. 2016;11(6):e0158460.
40. Lohith TG, Bennacef I, Vandenberghe R, Vandenbulcke M, Salinas CA, Declercq R, et al. Brain Imaging of Alzheimer Dementia Patients and Elderly Controls with ^{18}F-MK-6240, a PET Tracer Targeting Neurofibrillary Tangles. J Nucl Med. 2019;60(1):107–14.

41. Ossenkoppele R, Rabinovici GD, Smith R, Cho H, Scholl M, Strandberg O, et al. Discriminative Accuracy of [^{18}F]flortaucipir Positron Emission Tomography for Alzheimer Disease vs Other Neurodegenerative Disorders. JAMA. 2018;320(11):1151–62.
42. Ossenkoppele R, Smith R, Mattsson-Carlgren N, Groot C, Leuzy A, Strandberg O, et al. Accuracy of Tau Positron Emission Tomography as a Prognostic Marker in Preclinical and Prodromal Alzheimer Disease: A Head-to-Head Comparison Against Amyloid Positron Emission Tomography and Magnetic Resonance Imaging. JAMA Neurol. 2021;78(8):961–71.
43. Pascoal TA, Shin M, Kang MS, Chamoun M, Chartrand D, Mathotaarachchi S, et al. In vivo quantification of neurofibrillary tangles with [^{18}F]MK-6240. Alzheimers Res Ther. 2018;10(1):74.
44. Pascoal TA, Therriault J, Benedet AL, Savard M, Lussier FZ, Chamoun M, et al. ^{18}F-MK-6240 PET for early and late detection of neurofibrillary tangles. Brain. 2020;143(9):2818–30.
45. Brambilla M, Secco C, Dominietto M, Matheoud R, Sacchetti G, Inglese E. Performance Characteristics Obtained for a New 3-Dimensional Lutetium Oxyorthosilicate–Based Whole-Body PET/CT Scanner with the National Electrical Manufacturers Association NU 2-2001 Standard. J Nucl Med. 2005;46(12):2083–91.
46. Rausch I, Cal-Gonzalez J, Dapra D, Gallowitsch HJ, Lind P, Beyer T, et al. Performance evaluation of the Biograph mCT Flow PET/CT system according to the NEMA NU2-2012 standard. EJNMMI Phys. 2015;2(1):26.
47. van Sluis J, de Jong J, Schaar J, Noordzij W, van Snick P, Dierckx R, et al. Performance Characteristics of the Digital Biograph Vision PET/CT System. J Nucl Med. 2019;60(7):1031–6.
48. Wagatsuma K, Miwa K, Sakata M, Oda K, Ono H, Kameyama M, et al. Comparison between new-generation SiPM-based and conventional PMT-based TOF-PET/CT. Phys Med. 2017;42:203–10.
49. Fleisher AS, Pontecorvo MJ, Devous MD, Sr., Lu M, Arora AK, Truocchio SP, et al. Positron Emission Tomography Imaging With [^{18}F]flortaucipir and Postmortem Assessment of Alzheimer Disease Neuropathologic Changes. JAMA Neurol. 2020;77(7):829–39.
50. Lowe VJ, Lundt ES, Albertson SM, Min HK, Fang P, Przybelski SA, et al. Tau-positron emission tomography correlates with neuropathology findings. Alzheimers Dement. 2020;16(3):561–71.
51. Leuzy A, Smith R, Cullen NC, Strandberg O, Vogel JW, Binette AP, et al. Biomarker-Based Prediction of Longitudinal Tau Positron Emission Tomography in Alzheimer Disease. JAMA Neurol. 2022;79(2):149–58.
52. Pascoal TA, Benedet AL, Tudorascu DL, Therriault J, Mathotaarachchi S, Savard M, et al. Longitudinal 18F-MK-6240 tau tangles accumulation follows Braak stages. Brain. 2021;144(11):3517–28.
53. Leuzy A, Pascoal TA, Strandberg O, Insel P, Smith R, Mattsson-Carlgren N, et al. A multicenter comparison of [(18)F]flortaucipir, [(18)F]RO948, and [(18)F]MK6240 tau PET tracers to detect a common target ROI for differential diagnosis. Eur J Nucl Med Mol Imaging. 2021;48(7):2295–305.

54. Teng E, Manser PT, Sanabria Bohorquez S, Wildsmith KR, Pickthorn K, Baker SL, et al. Baseline [^{18}F]GTP1 tau PET imaging is associated with subsequent cognitive decline in Alzheimer's disease. Alzheimers Res Ther. 2021;13(1):196.
55. Jack CR Jr, Wiste HJ, Weigand SD, Therneau TM, Lowe VJ, Knopman DS, et al. Defining imaging biomarker cut points for brain aging and Alzheimer's disease. Alzheimers Dement. 2017;13(3):205–16.
56. Bun S, Moriguchi S, Tezuka T, Sato Y, Takahata K, Seki M, et al. Findings of ^{18}F-PI-2620 tau PET imaging in patients with Alzheimer's disease and healthy controls in relation to the plasma P-tau181 levels in a Japanese sample. Neuropsychopharmacol Rep. 2022;42(4):437–48.
57. Ossenkoppele R, Leuzy A, Cho H, Sudre CH, Strandberg O, Smith R, et al. The impact of demographic, clinical, genetic, and imaging variables on tau PET status. Eur J Nucl Med Mol Imaging. 2021;48(7):2245–58.
58. Dore V, Bohorquez SS, Leuzy A, Shimada H, Bullich S, Bourgeat P, et al. Towards a universal cortical tau sampling mask. Alzheimer's Dement. 2021;17:1.
59. Dore V, Bullich S, Bohorquez SS, Leuzy A, Shimada H, Rowe C, et al. CenTauR$_z$: A standardized quantification of tau PET scans. Alzheimer's Dement. 2022;18:1.
60. Verwer EE, Golla SSV, Kaalep A, Lubberink M, van Velden FHP, Bettinardi V, et al. Harmonisation of PET/CT contrast recovery performance for brain studies. Eur J Nucl Med Mol Imaging. 2021;48(9):2856–70.
61. Hoffman EJCP, Guerrero TM, et al. Assessment of accuracy of PET utilizing a 3-D phantom to simulate the activity distribution of [^{18}F]fluorodeoxyglucose uptake in the human brain. J Cereb Blood Flow Metab. 1991;11:A17–25.

Figures

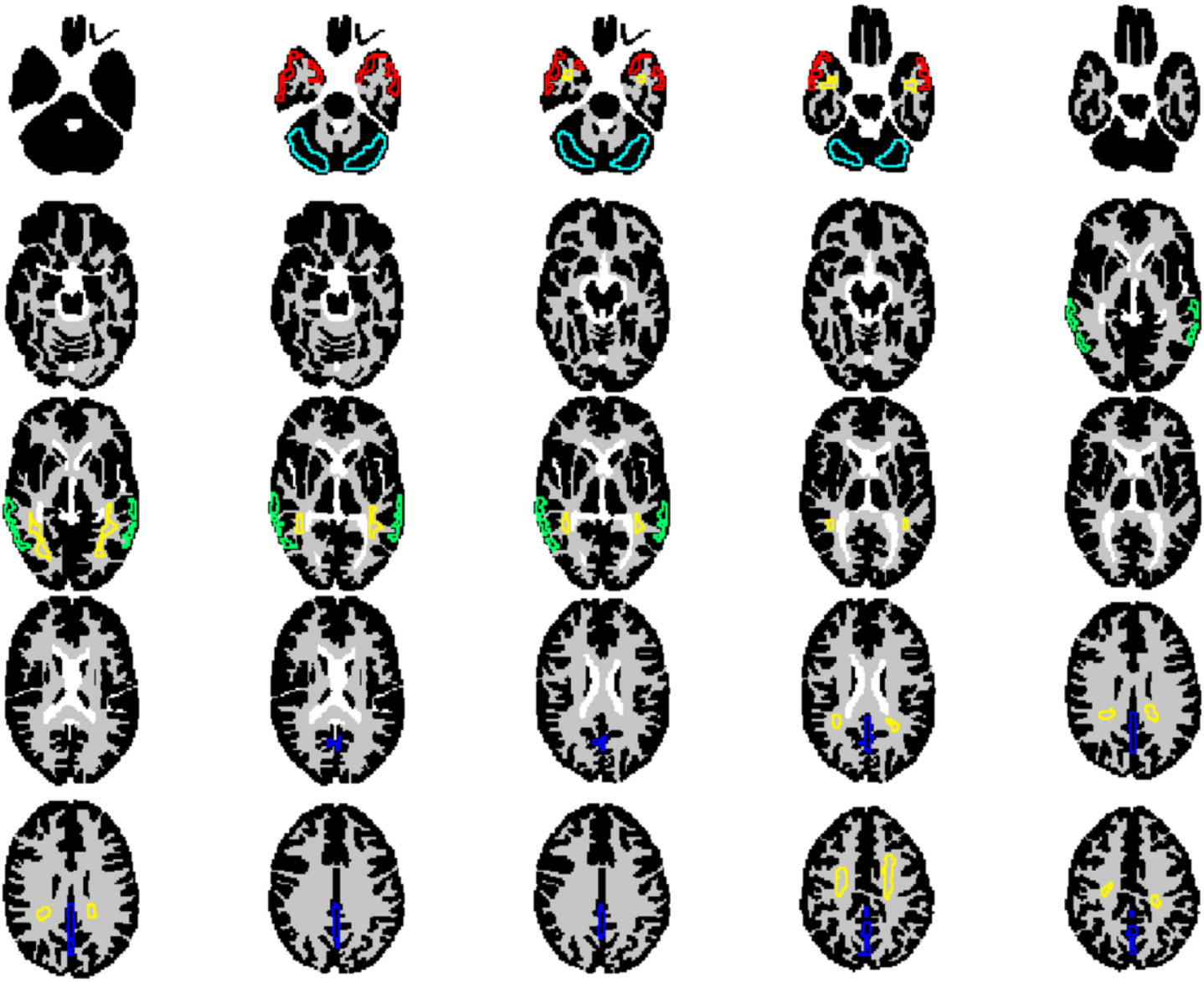

Figure 1

Volume-of-interest template for phantom tau PET images.

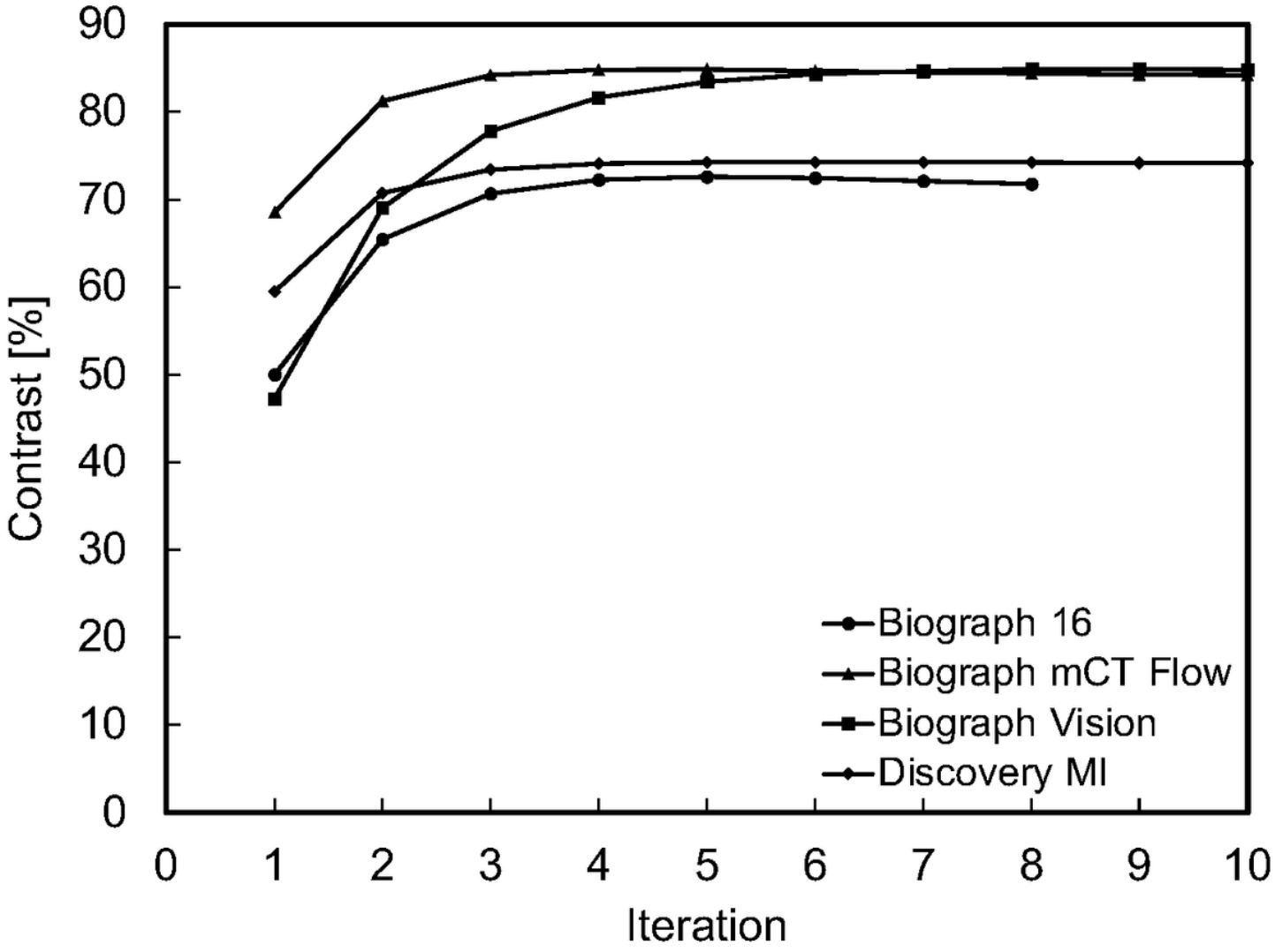

Figure 2

Contrast as a function of iterations in four scanners.

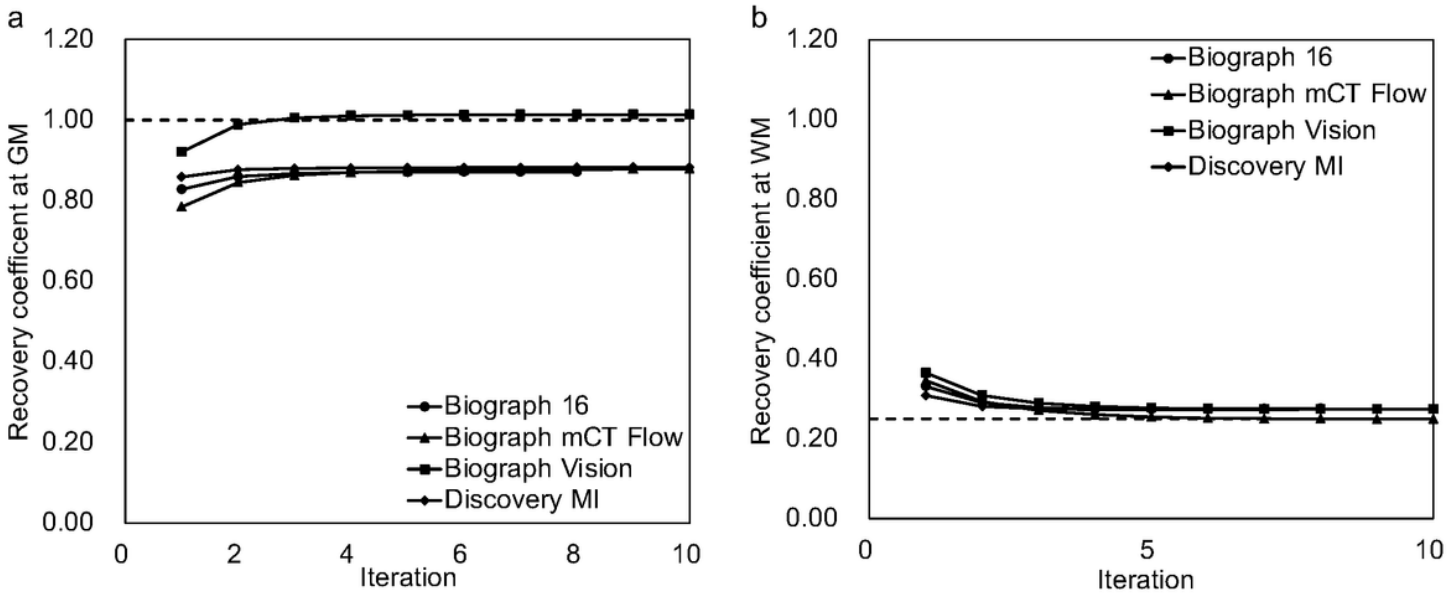

Figure 3

Recovery coefficients (RC) as functions of iterations in four scanners. (a) Grey matter (GM). (b) White matter (WM). Dashed lines, true activity (RC) = 1.0 in GM and 0.25 in WM.

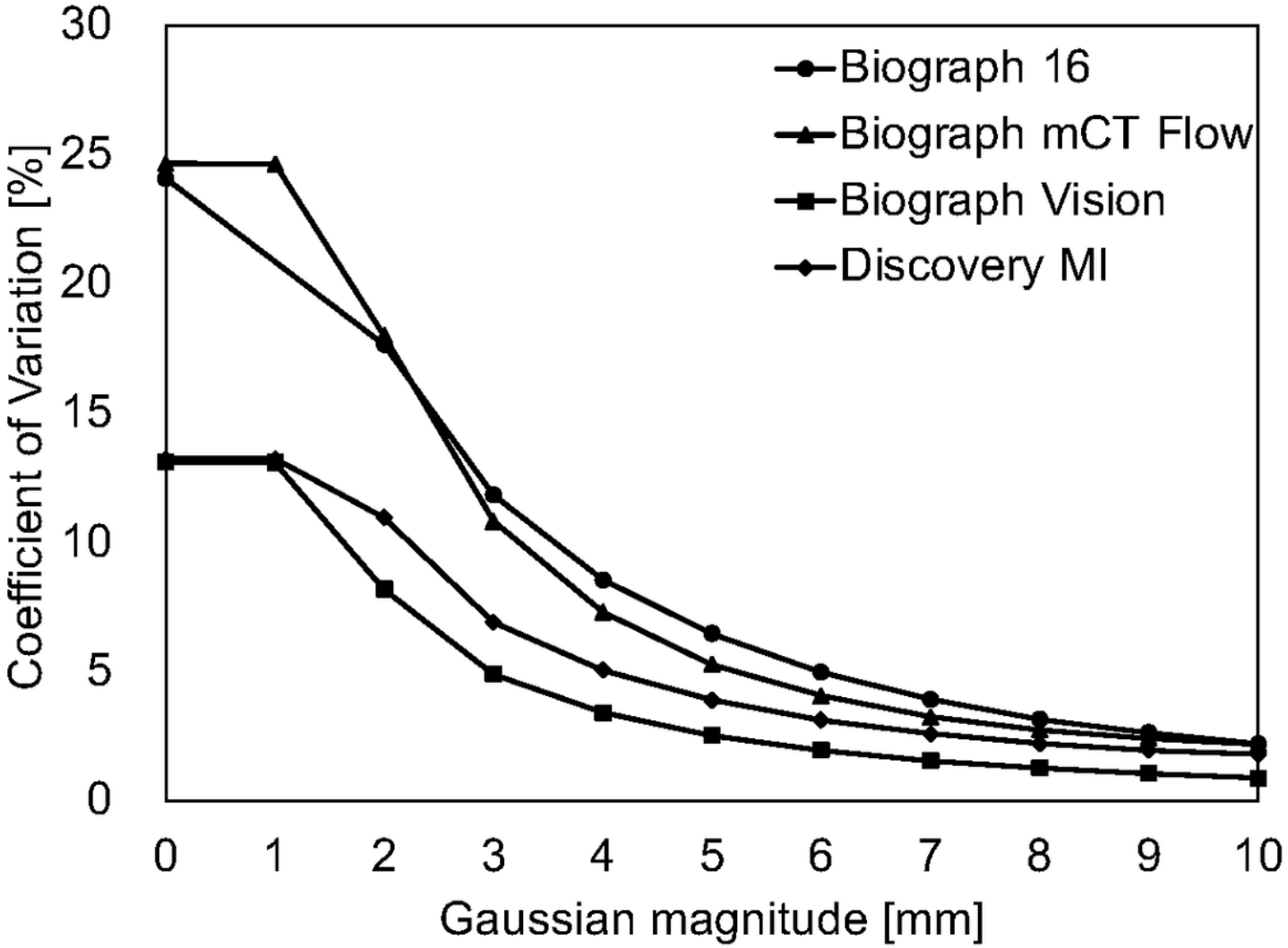

Figure 4

Magnitude of Gaussian filter in four scanners.

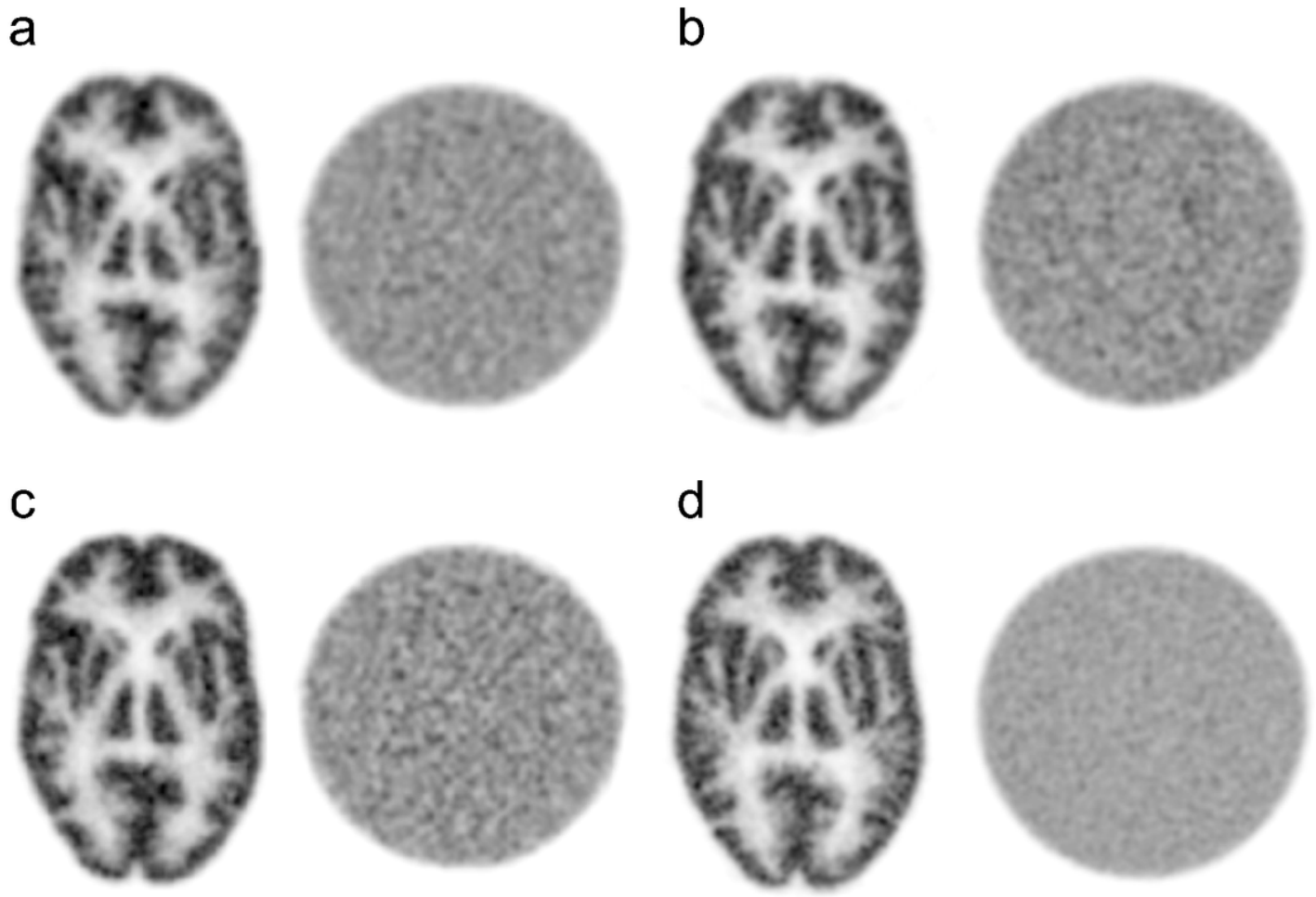

Figure 5

Brain and cylindrical phantom images acquired using four scanners and reconstructed under tau-specific conditions. Biograph 16 (a; It, 4; GF, 4 mm), Biograph mCT Flow (b; It, 4; GF, 4 mm), Biograph Vision (c; It, 4; GF, 3 mm), and Discovery MI (d; It, 4; GF, 3 mm). It, iteration; GF, Gaussian filter.